PAPER • **OPEN ACCESS**

Verified modeling of a low pressure hydrogen plasma generated by electron cyclotron resonance

To cite this article: F Sigeneger *et al* 2022 *Plasma Sources Sci. Technol.* **31** 105011

OPEN ACCESS
IOP Publishing
Plasma Sources Science and Technology
Plasma Sources Sci. Technol. **31** (2022) 105011 (13pp)
https://doi.org/10.1088/1361-6595/ac963e

Verified modeling of a low pressure hydrogen plasma generated by electron cyclotron resonance

F Sigeneger*, J Ellis[1], J Harhausen, N Lang and J H van Helden

Leibniz Institute for Plasma Science and Technology, Felix-Hausdorff-Str. 2, 17489 Greifswald, Germany

E-mail: sigeneger@inp-greifswald.de

Received 16 March 2022, revised 15 September 2022
Accepted for publication 29 September 2022
Published 28 November 2022

Abstract

A self-consistent fluid model has been successfully developed and employed to model an electron cyclotron resonance driven hydrogen plasma at low pressure. This model has enabled key insights to be made on the mutual interaction of microwave propagation, power density, plasma generation, and species transport at conditions where the critical plasma density is exceeded. The model has been verified by two experimental methods. Good agreement with the ion current density and floating potential—as measured by a retarding energy field analyzer—and excellent agreement with the atomic hydrogen density—as measured by two-photon absorption laser induced fluorescence—enables a high level of confidence in the validity of the simulation.

Keywords: hydrogen, plasma, ECR, fluid model, TALIF

(Some figures may appear in colour only in the online journal)

1. Introduction

Low pressure hydrogen plasmas are of great interest to a plethora of industrial sectors including multiple stages of semiconductor fabrication [1–4], diamond-like carbon film manufacturing [5, 6], and for their usage as a hydrogen radical source [7]. Equally, the interaction between a hydrogen plasma and a surface is of prominent importance in a number of academic research fields such as negative ion generation for neutral beam injection [8–10] and ammonia synthesis [11–13].

Numerous mechanisms can be used to generate the hydrogen plasma, however, the focus of this study is on microwave driven plasmas, specifically through the use of an electron cyclotron resonance (ECR) source. Recent developments include compact source designs with a static magnetic field; this provides a high power efficiency and importantly the ability to scale the plasma by employing matrix configurations of individual plasma sources [14–17].

ECR plasmas represent a very interesting subject of investigation and a challenge with respect to modeling because of the large variety of processes that need to be considered. In addition to the plasma description, the static magnetic field must be included as well as the propagation of the microwave field. All of these aspects are strongly coupled and require a self-consistent approach that takes into account the non-isotropic transport of charge carriers and the damping of microwave propagation due to the plasma.

The first models of ECR discharges have been published in the 1990s and were based on Monte Carlo simulations [18] or fluid approaches [19]. A series of investigations are devoted to describe electron cyclotron resonance ion sources (ECRIS). Because of the very low pressure and the large electron energy (up to several keV) particle methods such as particle in cell (PIC) or Monte Carlo have been used [20–22]. Partly, the particle methods are applied to the ion component only and electrons are taken as a neutralizing background

* Author to whom any correspondence should be addressed.
[1] Current address: Oxford Instruments Plasma Technology, Yatton, Bristol, United Kingdom

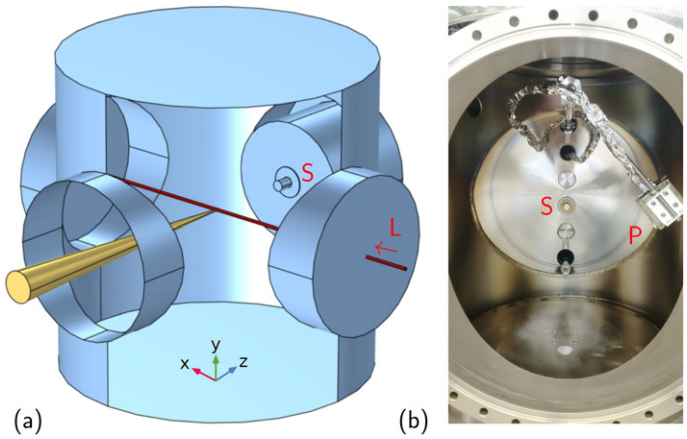

Figure 1. 3D CAD model of the process chamber together with the optical axes of the TALIF scheme (a). (L) denotes the axis of the UV laser beam, (S) the ECR source. The fluorescence light as seen by the detector unit in front of the window is depicted by the yellow cone. (b) A photo through the front flange showing the arrangement of the RFEA probe (P) within the chamber in a moved-off position with respect to the ECR source (S). During the RFEA measurements, the probe is situated on the axis defined by the center of the source S (z direction). Further details are given in figure 2.

with a given mean energy [21]. Recently, very time-consuming 3D PIC simulations of the electron component assuming ions as background have been published [22]. Only first steps to a self-consistent coupling with Maxwell's equations could be reached in this study due to the demanding particle simulations.

On the other hand, ECR plasmas in the pressure range of several Pa have been successfully described by fluid models. A self-consistent fluid model to describe an ECR plasma in argon with an iterated time integration of both the microwave and plasma equation and a semi-implicit Poisson method was published by Hagelaar *et al* [23]. This work is widely accepted as a basic reference for later modeling of ECR plasmas of this type. The authors reported results obtained with electron densities below and above the cut-off value of $n_c = 7.4 \times 10^{16}$ m^{-3} and the resultant changing damping of microwave propagation. Further ECR discharges in hydrogen [24] and argon [25] with electron densities lower than n_c were investigated by a fluid and hybrid model, respectively. The weak microwave damping enabled observations of the typical ECR behavior in these studies. Here, the maximum electron power gain occurs in the vicinity of the ECR surface, as characterized by the critical field strength $B_c = 875$ G of the static magnetic field.

The current investigations aim to achieve an accurate description of the hydrogen plasma driven by a compact, commercially available ECR source. A self-consistent fluid model is applied to investigate an ECR hydrogen plasma for larger values of power and electron density as typically produced by the ECR source under study. In particular, the interactions between microwave propagation and plasma generation with electron densities exceeding the cut-off value are analyzed. The competing effects of microwaves to increase electron density while impeding microwave propagation lead to complex spatial power density structures. The Maxwell equations describing the microwave are efficiently solved in the frequency domain in contrast to the time-dependent solution used in reference [23]. The strict solution of Poisson's equation yields correct spatial profiles of the plasma potential caused by space charges mainly occurring in the sheath which is important for the determination of ion fluxes. To verify the model, the results are compared with those obtained by two experimental methods. Firstly, a retarding field energy analyzer (RFEA) was used to measure the ion current and the floating potential. Secondly, two-photon absorption laser induced fluorescence (TALIF) was used to measure the absolute ground state atomic hydrogen density.

The paper is organized as follows: the setup and the diagnostic methods are described in section 2, details of the model are explained in section 3, results are presented and discussed in section 4, and a summary is given in section 5.

2. Setup and experiment

2.1. Process chamber

Experiments were conducted in a vacuum vessel with a volume of approximately 70 l. The chamber shape corresponds to a vertical cylinder with window flanges perpendicular to the axis, which provides diagnostic access for the RFEA and TALIF, respectively. Figure 1(a) shows schematically the 3D CAD model of the chamber.

Three flanges of the chamber are used for the application of TALIF. For further details, the reader is referred to section 2.3 below. When performing RFEA measurements the probe is positioned within the process chamber by means of a UHV-manipulator which is mounted on a modified back flange together with the ECR-source. The photo through the front flange in figure 1(b) illustrates the geometric arrangement of the RFEA in the chamber with respect to the ECR source, here presented in a moved-off position.

Base pressures of 2×10^{-4} Pa are achieved through a combination of a turbo molecular pump and a floor pump.

Operational pressures are controlled through a fixed gas flow, 100 sccm of hydrogen with a gas purity of 6.0, controlled by a mass flow controller. A feedback loop controls a gate valve with respect to the pressure, as measured by a Baratron gauge, that ensures consistent operational pressures.

The plasma is excited by a commercial microwave ECR source, Aura Wave from Sairem, mounted on the back flange; this source consists of a solid state microwave generator and a compact microwave launcher with coaxial geometry [17]. The Aura Wave source allows up to 200 W of microwave power to be coupled into a plasma in a pressure range of 3 to 10 Pa. The excitation frequency is variable in the range from 2.4 to 2.5 GHz which ensures minimized reflected microwave power for a given operation condition.

2.2. Retarding field energy analyzer

A home-made four-grid retarding field energy analyser [26–28] was used to investigate the ionic species within the plasma. Given the established diagnostic method only a brief description will be provided here. However, for a more detailed description of the diagnostic and measurement apparatus please refer to Harhausen *et al* [29]. A separate bias can be applied to the front electrode to use the RFEA as a planar probe. The floating potential V_f can be determined from the current voltage characteristics as measured by the front electrode. From this, an estimation for the ion current density at V_f can be calculated; this is conducted by adopting a model for the ion saturation current. Since no ion velocity distributions were extracted from the RFEA data for comparison to the model, the determination of the ion saturation current was conducted in this work by using a simplified linear extrapolation of the far ion saturation branch at floating potential V_f. Therefore, compared to the model calculations in section 4, the experimental ion current densities reflect an upper limit being overestimated by up to 30%, which is supported by the difference to a commonly used power law approach considering an expected sheath expansion according to e.g. [30]. Using such a model, the knowledge of the plasma potential is mandatory since the extrapolated ion current must vanish there. In contrast, the contribution of secondary electron emission to the ion current is expected to be in the range of a few percent of the measured value [26]. Furthermore, the uncertainty of the floating potential remains below the size of the symbols used in the figures. The housing of the RFEA probe has an edge length of 48 mm and a thickness of 20 mm. As such a macroscopic device it affects the plasma in its vicinity. Therefore, it is considered in the model by adopting a simplified cylindrical geometry.

For the measurements, the RFEA probe is positioned along the axis of symmetry of the ECR source at various distances in the range from 10 to 25 cm (z axis in figure 1(a)). Radial measurements, i.e. along the x axis as depicted in figure 1(a) are also possible but are not subject of the presented work here. For clarity, the position and size of the RFEA as taken into account in the model is drawn in the figures 2, 5, 7 and 9 as well. It is worth noting that the modeled current densities integrated over the entire front plate are comparable to those measured by the RFEA.

2.3. Two-photon absorption laser induced fluorescence

TALIF was used to measure atomic hydrogen densities within the plasma. Given the established method [31–34], only a brief description of the diagnostic will be given here. The principle mechanism of TALIF is that two photons are used to excite a ground state species into an upper level that then relaxes to a lower level and releases a photon in the process. By detecting the fluorescence photons produced during this relaxation, combined with knowledge of the reduced optical branching ratio and various invariant experimental terms, the density of the excited state can be calculated. This excited state density is proportional to the ground state density. However, a calibration, using a noble gas with a similar two-photon excitation scheme, is required to determine absolute ground state densities [31, 35].

Conducting TALIF to measure atomic hydrogen requires the creation of laser radiation with a wavelength of 205 nm. This was obtained through the combination of a frequency doubled Nd:YAG, Spectra Physics Quanta Ray, pump laser coupled into a Sirah Precision Scan SL dye laser. The 615 nm red light from the dye laser then underwent frequency doubling, through a BBO crystal, that was then remixed with residual red light from the dye laser in a second BBO crystal for sum-frequency generation to the required 205 nm radiation. The output of the laser is then attenuated via an attenuation scheme to ensure that no photo-ionisation events take place; saturation curve experiments showed that an energy per pulse of 370 and 19 μJ should be used for hydrogen and krypton, as the calibration gas, respectively. Effective lifetimes were measured to be 12 and 33 ns for hydrogen and krypton, respectively and were found to be invariant on any parametric variation conducted in this study.

The setup at the process chamber is depicted in figure 1(a). The injection of the UV laser pulses (L) was conducted along the x axis from the right flange to the left one both equipped with quartz windows. After transmission through the second flange window, the laser energy was diminished with the help of a beam dump. A small region of interest, approximately 10 by 2 mm, directly in front of the ECR source but with a separation of 115 mm from the source tip in z direction was chosen. For clarity, the position of the region of interest is depicted in figure 2 together with the RFEA probe. The detection of the fluorescence at 656 nm was performed in z direction as well using an Andor iStar DH734x iCCD camera combined with an appropriate spectral filter.

3. Model description

The model of the ECR plasma consists of three main parts: the description of (i) the static magnetic field caused by the permanent magnets, of (ii) the microwave and of (iii) the plasma. These parts are solved in an axially symmetric geometry which is shown in figure 2.

3.1. Static magnetic and microwave fields

The static magnetic flux density $\mathbf{B}^{\mathrm{s}}$ caused by the permanent magnets is determined using Maxwells equations according to

$$\mathbf{B}^{\mathrm{s}} = \mu_0(\mathbf{H}^{\mathrm{s}} + \mathbf{M}) \tag{1}$$

$$\nabla \times \mathbf{B}^{\mathrm{s}} = 0 \tag{2}$$

where μ_0, $\mathbf{H}^{\mathrm{s}}$ and $\mathbf{M}$ denote the vacuum permeability, the static magnetic field strength and the magnetization, respectively. The magnetization $\mathbf{M}$ is a specific material property of the permanent magnet which is related to the magnetic moment $\mathbf{m}$ of the magnet by $\mathbf{m} = \int_V \mathbf{M}\,\mathrm{d}V$. The static magnetic field $\mathbf{B}^{\mathrm{s}}$ is determined in advance because it is not influenced by the model parts (ii) and (iii).

The microwave fields $\mathbf{E}$ and $\mathbf{B}$ are described by Maxwell's equations

$$\nabla \times \mathbf{E} = -\frac{\partial \mathbf{B}}{\partial t} \tag{3}$$

$$\frac{1}{\mu_0}\nabla \times \mathbf{B} = \mathbf{J} = \mathbf{J}_{\mathrm{d}} + \mathbf{J}_{\mathrm{p}} \tag{4}$$

$$\mathbf{J}_{\mathrm{d}} = \varepsilon_0\varepsilon_{\mathrm{r}}\frac{\partial \mathbf{E}}{\partial t}, \tag{5}$$

with the vacuum permittivity μ_0, the vacuum permeability ε_0 and the relative permeability ε_{r}. The total current density $\mathbf{J}$ is the sum of the displacement current density $\mathbf{J}_{\mathrm{d}}$ and the plasma current density $\mathbf{J}_{\mathrm{p}}$. The latter can be approximated in the microwave time scale by the electron current density

$$\mathbf{J}_{\mathrm{p}} = -en_{\mathrm{e}}\mathbf{v}_{\mathrm{e}} \tag{6}$$

neglecting the slow motion of ions. Here, e, n_{e} and $\mathbf{v}_{\mathrm{e}}$ denote the charge, density and mean velocity of electrons, respectively. The mean electron velocity is obtained from electron momentum equation according to

$$\frac{\partial \mathbf{v}_{\mathrm{e}}}{\partial t} = -\frac{e}{m_{\mathrm{e}}}(\mathbf{v}_{\mathrm{e}} \times \mathbf{B}^{\mathrm{s}} + \mathbf{E}) - \nu_{\mathrm{m}}\mathbf{v}_{\mathrm{e}} \tag{7}$$

where ν_{m} denotes the frequency of electron momentum transfer in collisions with heavy particles.

The equations (3)–(5) are solved in the frequency domain by replacing all vectors $\mathbf{X} \equiv \mathbf{E}, \mathbf{B}, \mathbf{J}_{\mathrm{p}}, \mathbf{v}_{\mathrm{e}}$ with $\mathbf{X} = \bar{\mathbf{X}}\,\mathrm{e}^{\mathrm{i}\omega t}$. A Fourier transformation of equation (7) yields the velocity amplitude as

$$\bar{\mathbf{v}}_{\mathrm{e}} = -\frac{e}{m_{\mathrm{e}}(\nu_m + \mathrm{i}\omega)}(\bar{\mathbf{v}}_{\mathrm{e}} \times \mathbf{B}^{\mathrm{s}} + \bar{\mathbf{E}}). \tag{8}$$

This relation can be used to determine the conductivity $\boldsymbol{\sigma}$ according to

$$\bar{\mathbf{J}}_{\mathrm{p}} = -en_{\mathrm{e}}\bar{\mathbf{v}}_{\mathrm{e}} = \boldsymbol{\sigma} \cdot \bar{\mathbf{E}}. \tag{9}$$

The magnetic field $\mathbf{B}^{\mathrm{s}}$ leads to a tensorial conductivity $\boldsymbol{\sigma} = en_{\mathrm{e}}\boldsymbol{\mu}_{\mathbf{e}}$ with the related tensorial mobility $\boldsymbol{\mu}_{\mathbf{e}}$ which depends in cylindric coordinates (r, ϕ, z) according to

$$\boldsymbol{\mu}_{\mathrm{e}} = \frac{\tilde{\mu}_{\mathrm{e}}}{\tilde{\mu}_{\mathrm{e}}^{-2} + |\mathbf{B}^{\mathrm{s}}|^2} \tag{10}$$

$$\times \begin{bmatrix} {B_r}^2 + \tilde{\mu}_{\mathrm{e}}^{-2} & B_rB_\phi + B_z\tilde{\mu}_{\mathrm{e}}^{-1} & B_rB_z - B_\phi\tilde{\mu}_{\mathrm{e}}^{-1} \\ B_\phi B_r - B_z\tilde{\mu}_{\mathrm{e}}^{-1} & {B_\phi}^2 + \tilde{\mu}_{\mathrm{e}}^{-2} & B_\phi B_z + B_r\tilde{\mu}_{\mathrm{e}}^{-1} \\ B_zB_r + B_\phi\tilde{\mu}_{\mathrm{e}}^{-1} & B_zB_\phi - B_r\tilde{\mu}_{\mathrm{e}}^{-1} & {B_z}^2 + \tilde{\mu}_{\mathrm{e}}^{-2} \end{bmatrix}$$

on the static magnetic field strength $\mathbf{B}^{\mathrm{s}}$ and on the complex mobility

$$\tilde{\mu}_{\mathrm{e}} = \frac{e}{m_{\mathrm{e}}(\nu_{\mathrm{m}} + \mathrm{i}\omega)}. \tag{11}$$

Equations (3)–(5) with related variables in the frequency domain can be combined to the relation

$$\nabla \times \frac{1}{\mu_0}\nabla \times \bar{\mathbf{E}} = (\omega^2\varepsilon_0\varepsilon_{\mathrm{r}} - \mathrm{i}\omega\boldsymbol{\sigma}) \cdot \bar{\mathbf{E}} \tag{12}$$

which is used to determine the components $\bar{E}_r$, $\bar{E}_\phi$ and $\bar{E}_z$ of the microwave electric field amplitude $\bar{\mathbf{E}}$.

The power $\bar{Q}$ transferred from the microwave to the electrons can be determined by

$$\bar{Q} = \frac{1}{2}\mathrm{real}(\bar{\mathbf{J}} \cdot \bar{\mathbf{E}}^*) \tag{13}$$

where $\bar{\mathbf{E}}^*$ denotes the complex conjugate of $\bar{\mathbf{E}}$.

3.2. Plasma description

The plasma equations describe the temporal relaxation of species densities and the electrostatic potential ϕ which is related to the electrostatic field $\mathbf{E}^{\mathrm{s}}$ according to

$$\mathbf{E}^{\mathrm{s}} = -\nabla\phi \tag{14}$$

in timescales beyond the microwave period. The plasma equations comprise continuity equations

$$\frac{\partial}{\partial t}n_l + \nabla \cdot \boldsymbol{\Gamma}_l = S_l \tag{15}$$

for all species densities n_l with the source term S_l, the electron energy balance equation

$$\frac{\partial}{\partial t}n_\epsilon + \nabla \cdot \boldsymbol{\Gamma}_\epsilon = e_0\boldsymbol{\Gamma}_{\mathrm{e}} \cdot \nabla\phi + \bar{Q} + S_\epsilon \tag{16}$$

with the energy source term S_ϵ to determine the electron mean energy density $n_\epsilon = n_{\mathrm{e}}u_{\mathrm{m}}$ and Poisson's equation

$$-\nabla \cdot (\varepsilon_{\mathrm{r}}\varepsilon_0\nabla\phi) = \sum_l q_l n_l \tag{17}$$

with q_l being the charge of species l. The particle fluxes $\boldsymbol{\Gamma}_l$ and the electron energy flux $\boldsymbol{\Gamma}_\epsilon$ are driven according to

$$\boldsymbol{\Gamma}_l = \mathrm{sgn}(q_l)n_l\boldsymbol{\mu}_l \cdot \mathbf{E}^{\mathrm{s}} - \boldsymbol{D}_l \cdot \nabla n_l \tag{18}$$

$$\boldsymbol{\Gamma}\epsilon = -n_\epsilon\boldsymbol{\mu}_\epsilon \cdot \mathbf{E}^{\mathrm{s}} - \boldsymbol{D}_\epsilon \cdot \nabla n_\epsilon \tag{19}$$

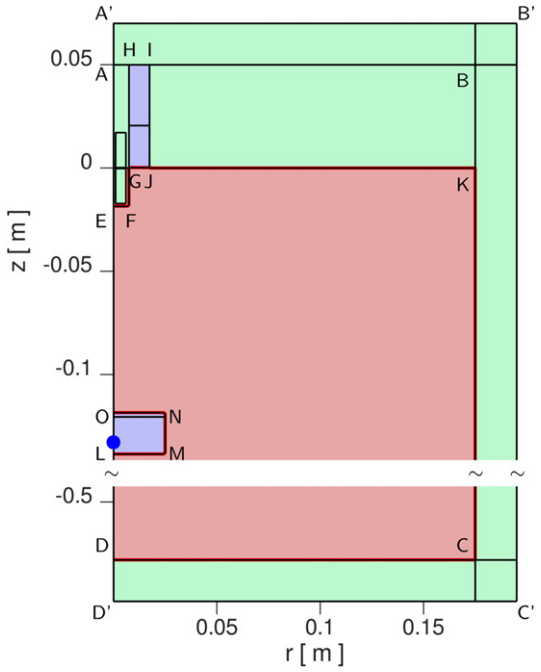

Figure 2. Solution region of the ECR reactor with the RFEA probe situated at $z_p \equiv |\mathsf{OE}| = 10$ cm. The region of interest for the TALIF measurements is depicted with the blue bullet •. To avoid overlapping, the RFEA probe is moved to the farmost position $z_\mathrm{p} = 25$ cm for the comparison with the TALIF data.

Table 1. Boundary conditions used in the plasma model with $\mathbf{n}$ denoting the outward directed normal vector.

Boundary	Condition
General	
AD	symmetry axis
Permanent magnetic field	
A'B'C'D'	$\mathbf{n}\cdot\mathbf{B}^\mathrm{s} = 0$
Microwave field	
HI	coaxial port in TEM mode with power P_port
EFGH,IJKCD	$\mathbf{n}\times\bar{\mathbf{E}} = 0$
Plasma equations	
EFGJKCD	$\phi = 0$
LMN	$-\mathbf{n}\cdot\mathbf{E}^\mathrm{s} = \sigma_\mathrm{s}/\varepsilon_0$
NO	$\phi = V_\mathrm{f}$
EFGJKCD,LMNO	flux conditions for all species ($\mathbf{\Gamma}_l$) and the electron energy flux $\mathbf{\Gamma}_\varepsilon$

by drift from the electrostatic field (first term) and diffusion (second term). The electron mobility $\boldsymbol{\mu}_\mathrm{e}$ is a real-valued tensor with components depending on the scalar mobility $\mu_0 = e/(m_\mathrm{e}\nu_\mathrm{m})$ and the static magnetic field $\mathbf{B}^\mathrm{s}$ which reads similar to equation (10) replacing $\tilde{\mu}_\mathrm{e}$ by μ_0. The electron diffusivity tensor $\boldsymbol{D}_\mathbf{e}$ is determined using Einstein's relation according to $\mathbf{D}_\mathbf{e} = \frac{k_\mathrm{B}T_\mathrm{e}}{e}\boldsymbol{\mu}_\mathbf{e}$. The corresponding electron transport coefficients for the energy transport are determined by the relations $\boldsymbol{\mu}_\epsilon = 5\boldsymbol{\mu}_\mathrm{e}/3$ and $\boldsymbol{D}_\epsilon = 5\boldsymbol{D}_\mathrm{e}/3$ [36].

Table 2. Surface reactions included in the plasma model.

Reaction	γ_f	γ_i	References
$\mathrm{H}\rightarrow 0.5\,\mathrm{H}_2$	0.1	—	[38]
$\mathrm{H}^+\rightarrow\mathrm{H}$	1	0.057	[39]
$\mathrm{H}_2^+\rightarrow\mathrm{H}_2$	1	0.06	[39]
$\mathrm{H}_3^+\rightarrow\mathrm{H}_2+\mathrm{H}$	1	0.086	[39]

The representations (18) and (19) are obtained from the momentum balance equations neglecting the inertia of the particles. While this assumption is justified for electrons, the approximation is limited for ionic species at low pressures. The authors are aware of possible limitations of the model at pressures of 5 Pa and below. Nevertheless, this assumption is required to prepare a numerically solvable model for the complex plasma situation.

The diffusion coefficients for the heavy species have been taken from literature [37] and Einstein's relation was used to determine the ion mobilities.

3.3. Reaction kinetics

The plasma model comprises electrons and the hydrogen species H, H^+, H_2^+ and H_3^+. The 34 reactions are listed with related references in table 3. The rate coefficients of the electron reactions are determined as functions of the mean electron energy u_m by solving the 0D Boltzmann equation with BOLSIG+ in version 03/2016 [36]. Furthermore, it is used to determine the electron momentum transfer frequency ν_m as function of the mean electron energy which is needed to prepare the plasma conductivity $\boldsymbol{\sigma}$ and the transport tensors $\boldsymbol{\mu}_\mathrm{e}$ and $\boldsymbol{D}_\mathrm{e}$.

Finally, the pumping of the gas that sustains the pressure is included as global loss rates $S_l^\mathrm{flow} = -\nu_l^\mathrm{flow} n_l$ for the species H, H^+, H_2^+ and H_3^+. The loss frequency ν_l^flow is determined from the gas flow rate Q^flow and the reactor volume V according to $\nu_l^\mathrm{flow} = Q^\mathrm{flow}/V$.

3.4. Boundary conditions

The solution domains in the axially symmetric geometry are shown in figure 2. The different model parts are solved on different domains as follows: The equation for the static magnetic field $\mathbf{B}^\mathrm{s}$ is solved on the extended region A′B′C′D′ (green shaded plus inner domains), the microwave field $\bar{\mathbf{E}}$ is determined on the domain EFGHIJKCDE (blue and red domains) and the plasma equations are solved on the red shaded domain EFGJKCDLMNOE. The RFEA probe (LMNO) is situated at a distance of $z_p \equiv |\mathsf{OE}|$ from the tip E of the source. The boundary conditions are listed in table 1. The microwave field is prescribed at boundary HI in TEM mode. Its power P_port is adjusted iteratively to fulfill the condition $P = \int_V \bar{Q}\,\mathrm{d}V$ where P is the total deposited power used as parameter for comparison with the experiment. The surface charge σ_s at the lower dielectric part (LMN) of the RFMA probe is determined by

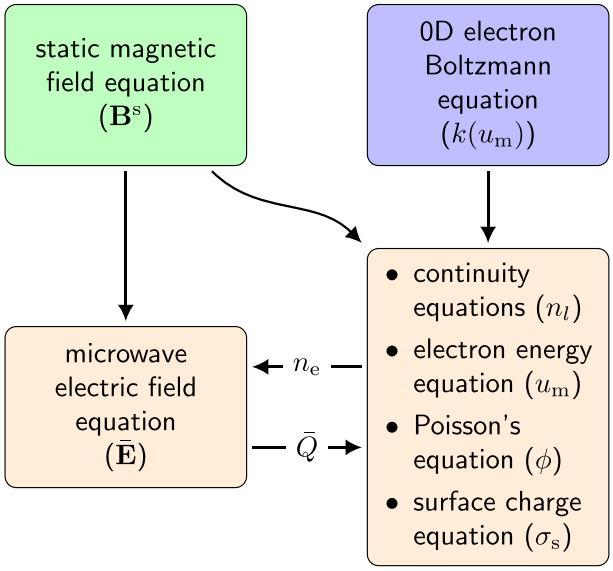

Figure 3. Scheme of the model algorithm illustrating the interactions between parts and equations.

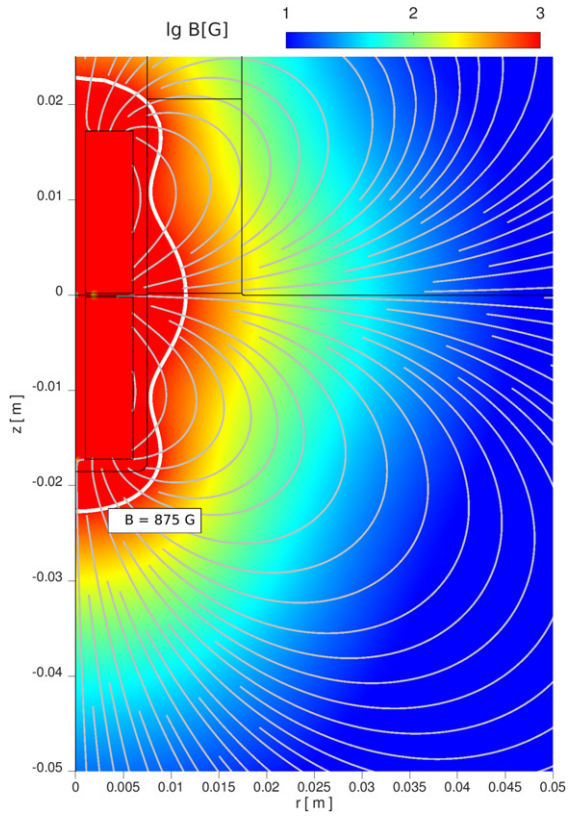

Figure 4. Magnetic field strength with the iso line marking $B_c = 875$ G.

$$\sigma_s = \sum_l \int_0^t \mathbf{n} \cdot \mathbf{\Gamma}_l(t')\mathrm{d}t'. \tag{20}$$

The floating potential V_f is adjusted so that the total electron and ion current to the metallic probe surface (NO) becomes zero.

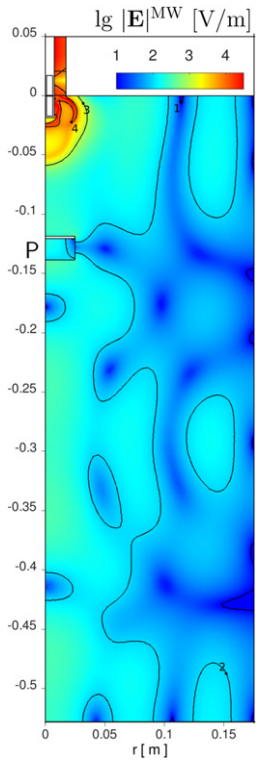

Figure 5. Magnitude of the microwave electric field strength. The influence of the RFEA probe denoted with P was taken into account.

The boundary conditions for the species densities incorporate the thermal velocity $v_l^{th} = \sqrt{(8k_B T_l)/(\pi m_l)}$ of respective species. The flux conditions for the electron particle flux $\mathbf{n} \cdot \mathbf{\Gamma}_e = \frac{1}{2} v_e^{th} n_e - \sum_l \gamma_l^{sec} (\mathbf{n} \cdot \mathbf{\Gamma}_l)$ and for the electron energy flux $\mathbf{n} \cdot \mathbf{\Gamma}_\varepsilon = \frac{5}{6} v_e^{th} n_\varepsilon - \sum_l \gamma_l^{sec} u^{sec} (\mathbf{n} \cdot \mathbf{\Gamma}_l)$ include secondary electron emission with the coefficients γ_l^{sec}. A mean energy of $u^{sec} = 5$ eV is assumed for the emitted electrons, however, the results of this model have been found to be relatively insensitive to this chosen value. For heavy particles, the condition $\mathbf{n} \cdot \mathbf{\Gamma}_l = \frac{1}{4}\left(\frac{\gamma_f}{1-\gamma_f/2}\right) v_l^{th} n_l + n_l \boldsymbol{\mu}_l \cdot \mathbf{E}^s$ is used which includes contributions from surface reactions described by sticking coefficients γ_f as well as migrative flux due to the static electric field. The surface reactions and related coefficients are listed in table 2.

As shown in figure 2, the regions for the RFEA and the TALIF measurements overlap. Therefore, the RFEA probe is moved to the farthest position $z_p = 25$ cm to enable a correct comparison with the TALIF data.

3.5. Numerical solution

Comsol multiphysics with the modules Plasma, RF and AC/DC is used to solve all equations of the model. For this purpose, an unstructured mesh with approximately 97 000 elements is prepared with refinements in the vicinity of the source and the probe. The solution of the model describes a temporal relaxation of the system over a period of 10 s. The interactions of different parts in the model, equations and variables as well as their dependencies are illustrated in figure 3. The stationary spatially homogeneous electron Boltzmann equation is solved

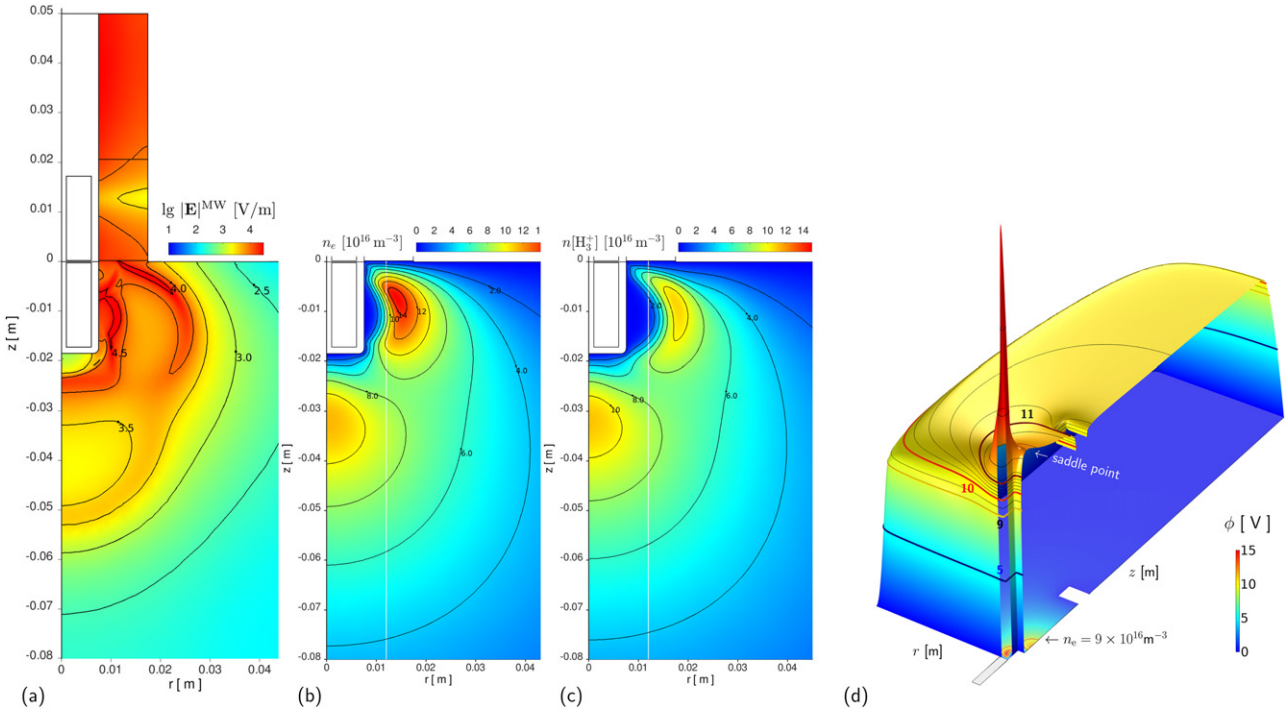

Figure 6. Magnitude of the microwave electric field strength around the ECR source (a), particle densities of electrons (b) and H_3^+ ions (c) and electrostatic potential (d). The white lines in (b) and (c) mark the axial cut with density profiles shown in figure 8. The surface at the base level in (d) represents the electron density as spectral plot with the labelled iso curve.

once to determine the rate coefficients k of reactions between electrons and heavy particle as functions of the mean energy u_m. The static magnetic field $\mathbf{B}^\mathrm{s}$ is determined for each geometric configuration (parameter z_p) in advance according to equations (1) and (2). The remaining equations describing the microwave (12) and the plasma (14)–(16), (20) are solved in a coupled system where the electron density n_e and the absorbed power $\bar{Q}$ determine the coupling between the microwave and plasma parts. Newton iterations are used to treat the nonlinear dependencies in each timestep as implemented internally in the time-dependent Comsol solver.

4. Results

Model calculations have been done for the reference case at a pressure of 7 Pa and an absorbed power of 100 W. The probe is situated at the position $z_\mathrm{p} = 10$ cm. Variations have been performed with respect to the probe position z_p, the pressure and the power. The flow rate is kept constant at a value of $Q^\mathrm{flow} = 100$ sccm.

4.1. Model results of the reference case

The magnetic field caused by the permanent magnets is shown in figure 4. The ECR condition for $\omega/(2\pi) = 2.45$ GHz is fulfilled along the white iso curve with $B_\mathrm{c} = \omega m_\mathrm{e}/e_0 = 875$ G. The comparison of this iso curve with that published for the Aura Wave source [40] allowed to determine the value for the magnetisation in equation (1) as $\mathbf{M} = 550$ kA m^{-1}.

The magnitude of the electric microwave field throughout the overall reactor volume is shown in figure 5 in logarithmic scale. The strong interaction of the plasma with the microwave causes the latter to reach only approximately 6 cm and 4 cm in the axial and radial directions, respectively. A strong damping by several orders of magnitude is obtained in the remote regions of the reactor.

A more detailed representation of the microwave field magnitude in the vicinity of the source is given by figure 6(a). This figure should be analyzed together with figures 6(b) and (c) which show the particle densities of electrons and H_3^+ ions, respectively. The electron density reaches a maximum of about 1.4×10^{17} m^{-3} which is beyond the cut-off density of $n_\mathrm{c} = 7.4 \times 10^{16}$ m^{-3}. Correspondingly, the electrical microwave field is strongly impeded in that region of enhanced electron density and is guided through the adjacent regions. Thus, the maxima of the electric microwave field amplitude up to about $|\mathbf{E}|^\mathrm{MW} = 7.5 \times 10^4$ V m^{-1} occur in the regions surrounding the maximum electron density where the lower density allows propagation of the microwave field. The contours of the electron density in figure 6(b) and consequently of the electric field in figure 6(a) reflect the dominant transport of the magnetized electrons and their energy along the direction of the static magnetic field $\mathbf{B}^\mathrm{s}$ as illustrated by the gray curves in figure 4.

A second maximum of the densities of electrons and H_3^+ ions is obtained near the discharge axis at approximately $z = -3.3$ cm. This maximum is not connected with an emphasized source at that position. On the contrary, the source term of electrons is negative at this position due to recombination

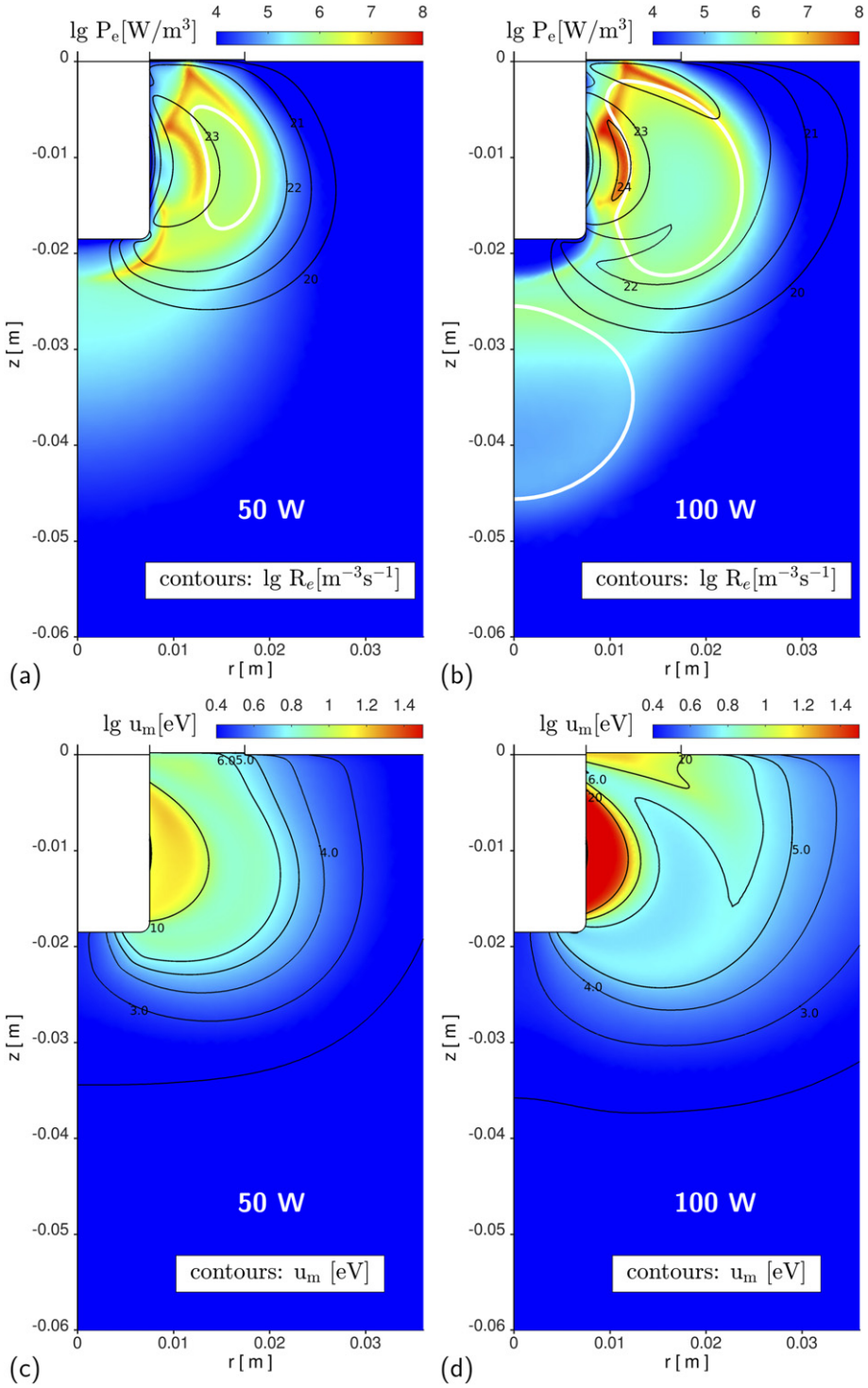

Figure 7. Quantities related to energy and ionization for a power of 50 W ((a) and (c)) and 100 W ((b) and (d)): electron power gain (spectral plots in (a) and (b)), ionization rate (black contours in (a) and (b)) and electron mean energy ((c) and (d)). The white contours in (a) and (b) mark the regions where the electron density exceeds the critical density n_c.

with H_3^+ ions. However, electrons are accumulated there because of a saddle point of the electrostatic potential and the resulting electron migration flux. This density maximum also influences the propagation of the microwave field as shown in figure 6(a).

The saddle point is a detail which is marked in figure 6(d). This figure shows the electrostatic potential in the whole reactor and iso curves of the electron density at the base level. A pronounced peak of the potential is obtained near the microwave source which is caused by the large charge carrier

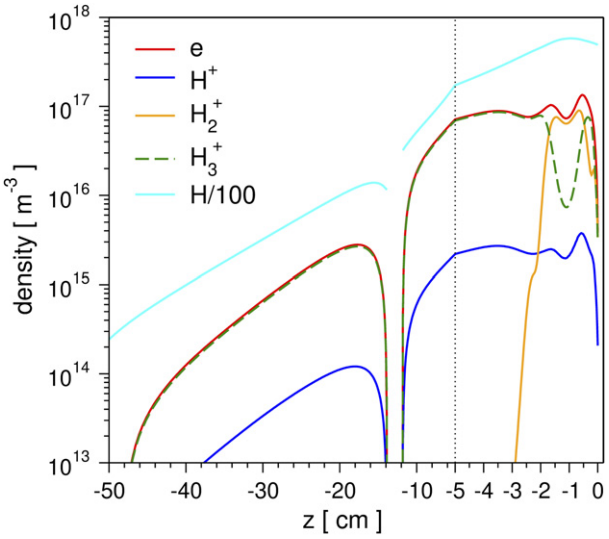

Figure 8. Species densities along the axial cut at $r = 12$ mm. The break below $z = -12$ cm is caused by the RFEA probe. The dotted vertical line marks a change in the scale of the ordinate.

density in that region and the resultant enhanced space charge density near the wall. Furthermore, the figure demonstrates the modification of the electrostatic potential due to the RFEA probe situated at $z_p = 10$ cm.

The interplay between electron density, power gain, ionization rate and mean electron energy is depicted in figure 7. Results for the reference case (100 W) are compared with those obtained for an absorbed power of 50 W. The white contours mark the regions where the electron density exceeds the cut-off value. The power is transferred to the electrons primarily in regions where the overlap of the microwave field strength and electron density reaches a maximum. The power gain causes an increased mean electron energy (figures 7(c) and (d)) and ionization rate (black contours in figures 7(a) and (b)). The transport of electron energy along the static magnetic field lines leads to pronounced spatial structures which coincide with the magnetic field lines as shown in figure 4. The comparison of both cases demonstrates the broadening of those regions where the electron density exceeds the cut-off value with increasing power. These regions represent voids for the propagation of the microwave and the related power gain for electrons.

Figure 8 shows the densities of the dominant species along the axial cut at $r = 12$ mm which is marked in figure 6 by white lines. For all species, a density decay of more than three orders of magnitude can be observed from the active region near the source at $z > -2$ cm in axial direction toward the reactor wall at $z \sim -53$ cm. The RFEA probe causes the depletion of all density profiles around its position ($z_p = 10$ cm). H_3^+ represents the dominant ion species in the remote regions of the reactor. This species is generated mostly due to the conversion reaction R28 ($H_2^+ + H_2 \rightarrow H_3^+ + H$) which also causes the rapid depletion of the H_2^+ ions in the active region at $z \sim -2.5$ cm. The H_3^+ ions are then transported mainly due to ambipolar diffusion from the active to the remote regions of the reactor. The H^+ ions are generated mainly due to the ionizing reactions R3 ($e + H_2 \rightarrow 2e + H + H^+$) and R27 ($e + H \rightarrow 2e + H^+$) and get rapidly converted to H_2^+ according to reaction R29 ($H_2 + H^+ \rightarrow H_2^+ + H$). The pronounced structure of electron density, power gain and mean energy as shown in figures 6 and 7 as well as the various reactions lead to multiple maxima of different species in the active region and considerable discrepancies in the density profiles across the axial direction.

Figure 9 summaries the key charged species particle flux onto the RFEA probe. The ion current density in the vicinity of the probe is shown in figure 9(a) by a spectral and an arrow plot. The magnitude of the ion flux becomes large at the metallic corner of the probe due to the increased electric field strength. This enhancement up to 230 μA m^{-2} can also be observed in figure 9(b) that shows the flux of charge carriers onto the surface of the RFEA probe. The ion flux is mainly driven by the dominant H_3^+ ions. The electron flux has an opposite radial profile because it is driven due to diffusion against the retarding electrostatic field.

4.2. Comparison with experimental results

The average of the calculated ion flux over the metallic surface of the RFEA probe can be compared with corresponding results obtained experimentally with the RFEA probe shown in figure 1(b). This comparison is shown in figure 10. The RFEA probe is used at the floating potential in the experiment and in the model. Good agreement has been obtained with respect to the relative dependence of the current density on the distance z_p between source tip and probe and with respect to the pressure. The differences in absolute values may be caused by the limitations of the applied drift–diffusion approximation at this low pressure. In addition, the deviation between the real quadratic shape of the probe and the necessarily cylindrical approximation in the model may lead to further discrepancies. Furthermore, as discussed in section 2.2, some uncertainties from the experimental side come from the extrapolation of the ion current to floating potential.

Both methods also deliver the potential of the floating probe. The comparison of its dependence on the position z_p is presented in figure 11 showing a very good agreement. Only a slight dependence on the position has been obtained theoretically and experimentally. The relative deviation between both results amounts to approximately 27% and 7% at 5 and 7 Pa, respectively. The increasing deviation with decreasing pressure is seen to be attributed to the limitations of the model at low pressures because of the drift-diffusion approximation used for the ion momentum.

The calculated and measured dependence of the ion current on the power for a pressure of 7 Pa is shown in figure 12. Apart from the deviation in absolute values already discussed, the same dependence was obtained in both methods. Furthermore, the figure 12 gives information on the dependence of the contribution of H_3^+ and H^+ ions to the total current. The current of both species onto the probe surface increase similarly with the

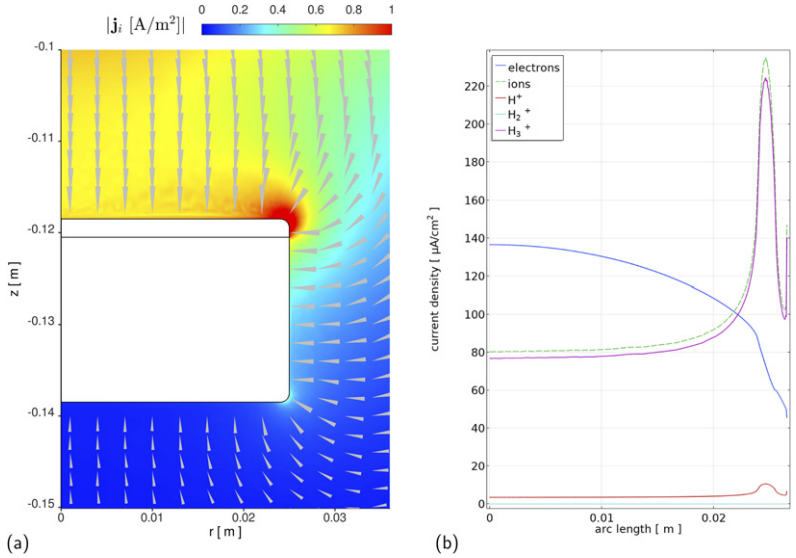

Figure 9. Ion current density around the RFEA probe with the metallic surface of the front plate (a) and spatial profile of current densities toward the metallic surface (b). The ordinate arc length denotes the path along the metallic surface of the probe on the cut shown in (a).

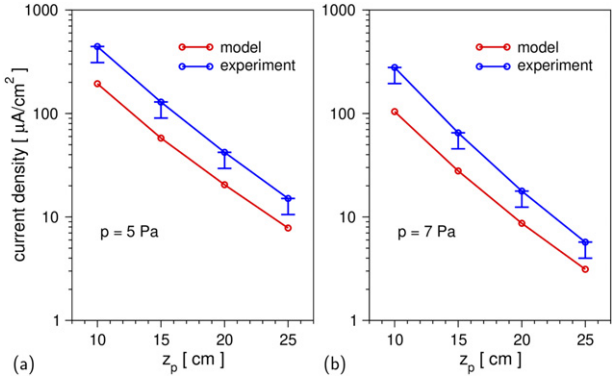

Figure 10. Comparison of calculated and measured results for the probe current density at 5 Pa (a) and 7 Pa (b).

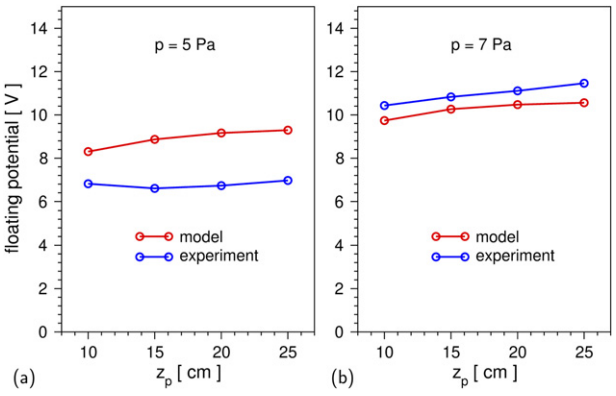

Figure 11. Comparison of calculated and measured results for the floating potential at 5 Pa (a) and 7 Pa (b).

power keeping H_3^+ as the dominant contribution which almost entirely compensates the electron current.

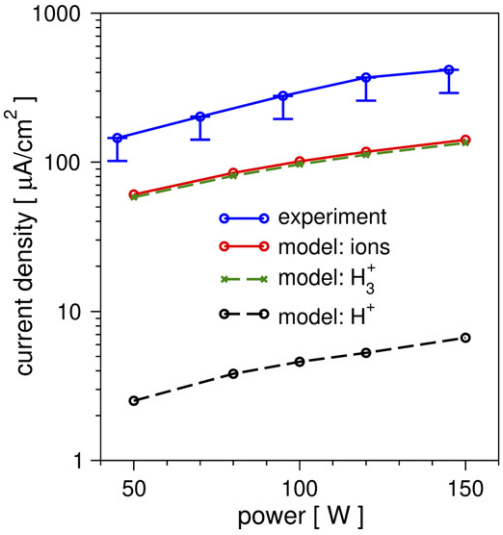

Figure 12. Comparison of the calculated and measured dependence of the probe current on power for the probe position $z_p = 10$ cm and a pressure of 7 Pa.

The comparison of the calculated and measured density of hydrogen atoms on the axis at $z = -13.35$ cm is shown in figure 13. Note that the RFEA probe is moved to the farthest position $z_p = 25$ cm for this comparison in the model. The relative deviation between both results amounts to approximately 27% and 8% at 5 and 7 Pa, respectively. This reflects the same increasing deviation between model and experiment for low pressures as in the above described findings on the floating potential. The slope of the power dependence obtained theoretically and experimentally deviate by approximately 10% from each other in both cases. The very good agreement with respect to absolute values and the dependence on power and pressure represents a convincing validation of model and experiment.

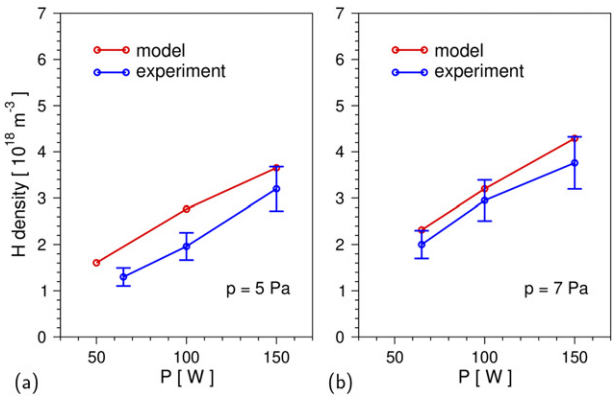

Figure 13. Comparison of calculated and measured H density at $r = 0$, $z = -13.35$ cm for 5 Pa (a) and 7 Pa (b).

5. Summary

The complex physics involved in a low-pressure hydrogen discharge driven by a commercial ECR source has been investigated by a self-consistent fluid model and validated by experimental investigations using both RFEA and TALIF measurements. This plasma source is characterized in its operating range for pressure and power by locally extended regions where the electron density exceeds the cut-off density. The model includes equations for the permanent magnetic field and the microwave field and fluid equations to describe the plasma generation. The strict solution of Poisson's equation yields correct spatial profiles of the plasma potential which is important for the determination of ion fluxes. The strong coupling between the microwave propagation, the power supply to the plasma and the damping of the microwave by the plasma becomes obvious in the results of the model. It leads to highly structured spatial profiles of the microwave electric field, the electron power gain, mean electron energy, and the electrostatic potential. These structures are largely determined by the field lines of the static magnetic field and the resultant transport of the magnetized electrons and their energy which is included in the model by a tensorial representation of the electron transport coefficients. The model also takes into account the influence of an RFEA probe consisting of conducting and dielectric parts that allows the comparison of measured ion current densities and floating potential with the model results.

Good agreement was obtained with respect to the dependence of the ion flux on the probe position, pressure, and power, respectively. The deviation with respect to absolute numbers may be caused by the limitation of the model at low pressure because of the drift–diffusion approximation for the ion momentum. In addition, the deviation between the real quadratic shape of the probe and the necessarily cylindrical approximation in the model may lead to further discrepancies. Furthermore, an exceptional agreement was obtained in the second verification of the model through comparison of atomic hydrogen densities results with the TALIF measurements. This twice-fold experimental validation yields a high-level of confidence in the physical solutions of the model and in the selection of the relevant chemical interactions chosen.

Future work will focus on an incorporation of more complex chemical interactions, an expansion of the relevant surface chemistry, and further experimental comparisons to maintain the current high-level of confidence in the models validity.

Acknowledgments

The authors acknowledge D Köpp for his skillful technical assistance. We thank D Loffhagen for providing useful discussions and his general support of the investigations.

Data availability statement

The source data for figures 8 and 10–13 are provided under DOI:10.34711/inptdat.599 in the public repository INPTDAT [47].

Appendix

Table 3. Reactions included in the plasma model. The dimensions of the rate coefficients are (m^3 s^{-1}) for two-body reactions and (m^6 s^{-1}) for three-body reactions. The electron temperature $T_e = (2/3)u_m$ and the heavy particle temperature T_g are specified in (K).

No.	Reaction	Rate coefficient	Threshold [eV]	References
	Elastic collisions			
1	$e + H_2 \rightarrow e + H_2$	$f(u_m)$	0.00	[41]
	Ionizing collisions			
2	$e + H_2 \rightarrow 2e + H_2^+$	$f(u_m)$	15.42	[42]
3	$e + H_2 \rightarrow 2e + H + H^+$	$f(u_m)$	18.15	[42]
4	$e + H_2 \rightarrow 2e + H + H^+$	$f(u_m)$	30.60	[42]
	Exciting collisions			
5	$e + H_2 \rightarrow e + H_2(v = 1)$	$f(u_m)$	0.52	[41]
6	$e + H_2 \rightarrow e + H_2(v = 2)$	$f(u_m)$	1.00	[41]
7	$e + H_2 \rightarrow e + H_2(v = 3)$	$f(u_m)$	1.50	[41]
8	$e + H_2(J = 0) \rightarrow e + H_2(J = 2)$	$f(u_m)$	0.04	[41]
9	$e + H_2(J = 1) \rightarrow e + H_2(J = 3)$	$f(u_m)$	0.07	[41]
10	$e + H_2 \rightarrow e + H_2$	$f(u_m)$	12.75	[42]
11	$e + H_2 \rightarrow e + H_2$	$f(u_m)$	13.29	[42]
12	$e + H_2 \rightarrow e + H_2$	$f(u_m)$	11.72	[42]
13	$e + H_2 \rightarrow e + 2H$	$f(u_m)$	7.93	[42]
14	$e + H_2 \rightarrow e + H_2$	$f(u_m)$	11.72	[42]
15	$e + H_2 \rightarrow e + H_2$	$f(u_m)$	13.60	[42]
16	$e + H_2 \rightarrow e + H_2$	$f(u_m)$	13.00	[42]
17	$e + 2H \rightarrow e + 2H$	$f(u_m)$	15.00	[41]
18	$e + 2H \rightarrow e + 2H$	$f(u_m)$	15.20	[41]
	Recombination			
19	$e + H_3^+ \rightarrow H_2 + H$	$f(u_m)$	0.00	[42]
20	$e + H_3^+ \rightarrow 3H$	$f(u_m)$	0.00	[42]
	Elastic collisions			
21	$e + H \rightarrow e + H$	$f(u_m)$	0.00	[43]
	Exciting collisions			
22	$e + H \rightarrow e + H(2p)$	$f(u_m)$	10.21	[43]
23	$e + H \rightarrow e + H(2s)$	$f(u_m)$	10.21	[43]
24	$e + H \rightarrow e + H(n = 3)$	$f(u_m)$	12.11	[43]
25	$e + H \rightarrow e + H(n = 4)$	$f(u_m)$	12.76	[43]
26	$e + H \rightarrow e + H(n = 5)$	$f(u_m)$	13.11	[43]
	Ionizing collisions			
27	$e + H \rightarrow 2e + H^+$	$f(u_m)$	13.61	[43]
	Heavy particle collisions			
28	$H_2^+ + H_2 \rightarrow H_3^+ + H$	2.11×10^{-15}		[44]
29	$H_2 + H^+ \rightarrow H_2^+ + H$	1.19×10^{-28}		[45]
30	$H_2 + H \rightarrow 2H + H$	$3.7 \times 10^{-16} \exp(-48300/T_g)$		[46]
31	$3H \rightarrow H_2 + H$	$8.3 \times 10^{-45} (T_g/300)^{-1}$		[46]
32	$H_2 + H_2 \rightarrow 2H + H_2$	$3.7 \times 10^{-16} \exp(-48300/T_g)$		[46]
33	$2H + H_2 \rightarrow H_2 + H_2$	$8.3 \times 10^{-45} (T_g/300)^{-1}$		[46]
	Recombination			
34	$e + H_2^+ \rightarrow H + H$	$3 \times 10^{-14} (300/T_e)^{0.5}$		[46]

ORCID iDs

F Sigeneger https://orcid.org/0000-0002-7238-6112
J Ellis https://orcid.org/0000-0002-9480-3407
N Lang https://orcid.org/0000-0002-5879-2210
J H van Helden https://orcid.org/0000-0001-8925-2607

References

[1] Shibata T, Nanishi Y and Fujimoto M 1990 *Japan. J. Appl. Phys.* **29** L1181
[2] Kondo N, Nanishi Y and Fujimoto M 1992 *Japan. J. Appl. Phys.* **31** L913
[3] Minami T, Miyata T, Iwamoto A, Takata S and Nanto H 1988 *Japan. J. Appl. Phys.* **27** L1753
[4] Sasaki K and Takada T 1998 *Japan. J. Appl. Phys.* **37** 402
[5] Lili R, Jianjun H, Liang G and Bing Q 2010 *Plasma Sci. Technol.* **12** 551
[6] Baudrillart B, Nave A, Hamann S, Bénédic F, Lombardi G, van Helden J H, Röpcke J and Achard J 2017 *Diam. Relat. Mater.* **71** 53
[7] Shimabukuro Y, Takahashi H, Iwamoto S, Tanaka K and Wada M 2020 *Plasma Sources Sci. Technol.* **29** 015005
[8] Aleiferis S, Svarnas P, Béchu S, Tarvainen O and Bacal M 2018 *Plasma Sources Sci. Technol.* **27** 075015
[9] Bentounes J *et al* 2018 *Plasma Sources Sci. Technol.* **27** 055015
[10] Fukumasa O and Matsumori M 1999 *Japan. J. Appl. Phys.* **38** 4581
[11] Bletzinger P and Ganguly B 1995 *Chem. Phys. Lett.* **247** 584
[12] Body T, Cousens S, Kirby J and Corr C 2018 *Plasma Phys. Control. Fusion* **60** 075011
[13] Ellis J, Köpp D, Lang N and van Helden J H 2021 *Appl. Phys. Lett.* **119** 241601

[14] Lacoste A, Lagarde T, Béchu S, Arnal Y and Pelletier J 2002 *Plasma Sources Sci. Technol.* **11** 407
[15] Latrasse L, Lacoste A, Sirou J and Pelletier J 2007 *Plasma Sources Sci. Technol.* **16** 7
[16] Rayar M, Le Quoc H, Lacoste A, Latrasse L and Pelletier J 2009 *Plasma Sources Sci. Technol.* **18** 025013
[17] Latrasse L, Radoiu M, Lo J and Guillot P 2017 *J. Microw. Power Electromagn. Energy* **50** 308
[18] Weng Y L and Kushner M J 1992 *J. Appl. Phys.* **72** 33
[19] Hemmers D, David M, Kempkens H and Uhlenbusch J 1998 *J. Phys. D: Appl. Phys.* **31** 2155
[20] Mascali D, Neri L, Celona L, Castro G, Torrisi G, Gammino S, Sorbello G and Ciavola G 2014 *Rev. Sci. Instrum.* **85** 02A511
[21] Mironov V, Bogomolov S, Bondarchenko A, Efremov A and Loginov V 2015 *Phys. Rev. Spec. Top. Accel. Beams* **18** 123401
[22] Mascali D, Torrisi G, Neri L, Sorbello G, Castro G, Celona L and Gammino S 2015 *Eur. Phys. J.* D **69** 27
[23] Hagelaar G J M, Makasheva K, Garrigues L and Boeuf J-P 2009 *J. Phys. D: Appl. Phys.* **42** 194019
[24] Liu Y G, Ke J L, Zhao G Y, Lou B-C, Hu Y H and Liu R 2018 *Nucl. Sci. Tech.* **29** 126
[25] Zhang B and Zhang X 2020 *Vacuum* **174** 109215
[26] Böhm C and Perrin J 1993 *Rev. Sci. Instrum.* **64** 31
[27] Baloniak T, Reuter R and von Keudell A 2010 *J. Phys. D: Appl. Phys.* **43**
[28] Conway G D, Perry A J and Boswell R W 1998 *Plasma Sources Sci. Technol.* **7** 337
[29] Harhausen J, Brinkmann R P, Foest R, Hannemann M, Ohl A and Schröder B 2012 *Plasma Sources Sci. Technol.* **21** 035012
[30] Chung P M, Talbot L and Touryan K J 1975 *Electric Probes in Stationary and Flowing Plasmas: Theory and Application* (Berlin: Springer)
[31] Niemi K, Gathen V S and Döbele H F 2001 *J. Phys. D: Appl. Phys.* **34** 2330
[32] Stancu G D 2020 *Plasma Sources Sci. Technol.* **29** 054001
[33] Goehlich A, Kawetzki T and Döbele H F 1998 *J. Chem. Phys.* **108** 9362
[34] Ellis J, Branson J, Niemi K, Wagenaars E and Gans T 2020 *J. Phys. D: Appl. Phys.* **53** 485202
[35] Schmidt J B, Roy S, Kulatilaka W D, Shkurenkov I, Adamovich I V, Lempert W R and Gord J R 2016 *J. Phys. D: Appl. Phys.* **50** 015204
[36] Hagelaar G J M and Pitchford L C 2005 *Plasma Sources Sci. Technol.* **14** 722
[37] Ellis H W, McDaniel E W, Albritton D L, Viehland L A, Lin S L and Mason E A 1978 *At. Data Nucl. Data Tables* **22** 179
[38] Hassouni K, Grotjohn T A and Gicquel A 1999 *J. Appl. Phys.* **86** 134
[39] Raizer Y P 1991 *Gas Discharge Physics* (Berlin: Springer)
[40] Boivin S, Glad X, Latrasse L, Sarkissian A and Stafford L 2018 *Phys. Plasmas* **25** 093511
[41] Phelps A V Phelps database http://lxcat.net (retrieved on 24 May 2019).
[42] Janev R K, Reiter D and Samm U 2003 *Ber. Forschungszent. Juelich* **4105** 188
[43] Alves L L 2014 *J. Phys. Conf. Series* **565** 1
[44] Bowers M T, Elleman D D and King J 1969 *J. Chem. Phys.* **50** 4787
[45] Méndez I, Gordillo-Vázquez F J, Herrero V J and Tanarro I 2006 *J. Phys. Chem* A **110** 6060
[46] Capitelli M, Ferreira C M, Gordiets B F and Osipov A I 2000 *Plasma Kinetics in Atmospheric Gases* (Berlin: Springer)
[47] Sigeneger F, Ellis J, Harhausen J, Lang N and van Helden J P 2022 Verified modeling of a low pressure hydrogen plasma generated by electron cyclotron resonance—dataset *INPTDAT* (available at: https://doi.org/10.34711/inptdat.599)